Supplement of Atmos. Chem. Phys., 26, 135–154, 2026
https://doi.org/10.5194/acp-26-135-2026-supplement

Atmospheric Chemistry and Physics
Open Access

Supplement of

Strong primary contribution to brown carbon light absorption in Tibet and urban areas: insights based on in situ measurements

Wenhui Zhao et al.

Correspondence to: Weiwei Hu (weiweihu@gig.ac.cn) and Shan Huang (shanhuang_eci@jnu.edu.cn)

S1. Positive matrix factorization (PMF) analysis

SP-AMS is based on the design of a high-resolution time-of-flight aerosol mass spectrometer (HR-ToF-AMS) (Decarlo et al., 2006), while SP-AMS has an additional Nd-YAG intra-cavity infrared (IR) laser module at the wavelength of 1064nm (Onasch et al., 2012). In this study, the SP-AMS at YBJ site was operated at 4 min alternating intervals between tungsten-only vaporizer mode (TV mode) and dual-vaporizer mode (DV mode), implemented by alternately activating (IR laser-on, i.e., dual vaporizers) and deactivating the laser vaporizer (IR laser-off, i.e., tungsten vaporizer only). In TV mode, the SP-AMS performs identically to the HR-ToF-AMS, providing continuous high-resolution mass concentration and mass spectral data for non-refractory submicron particulate matter (NR-PM_1). In DV mode, simultaneous use of both vaporizers enables real-time quantification of refractory black carbon (rBC) and NR-PM_1. rBC absorbs strongly at 1064nm and consequently heats up to ～ 4000 ℃ for rBC vaporization (Onasch et al., 2012). The term rBC is operationally defined, referring to BC particles detected by SP-AMS. However, the data for the PMF analysis in this study originated exclusively from the tungsten-vaporizer mode (the data for dual-vaporizer mode will be discussed in Liang et al. in preparation). Thus, the positive matrix factorization (PMF) was performed on the high-resolution mass spectra of organic aerosol (OA) of the SP-AMS operated with tungsten-only vaporizer at the YBJ site. Figure S2 is the standard determination panel for separating the PMF factors. The solutions of factor 1–8 with fpeak varied from -1 to 1 were run. The Q/Q_{exp}, scaled residuals, comparison between mass spectra of individual factors, diurnal variation of each factor, and comparison of the temporal evolution of every factor with corresponding external tracers were used to identify the best correlation for determining the optimum number of factors. The detailed steps were listed in a previous study (Zhang et al., 2011). The sharp decrease of Q/Q_{exp} suggest there are mass was not resolved out when 2-factor solutions were chosen. Values of $Q/Q_{exp} >> 1$ indicate either an underestimation of the errors or the presence of variability in the factor mass spectra that cannot be adequately modeled by the sum of the given number of factors. $Q/Q_{exp} << 1$ indicates overestimation of the errors of the input data (Ulbrich et al., 2009). In this study, Q/Q_{exp} =0.82 under the final PMF result of 5-factor solution is within an acceptable range. Table S1 summarized the descriptions of PMF solutions. In general, the 5-factor solution is the optimum solution. For 4-factor solution, we found mixed factor between BBOA and Biofuel OA. For 6-10 factor solution, we found there is an extra factor with unexplained peak (m/z 77) in their spectrum. As shown in Fig. S2, 5–factors solution (fpeak = 0) is the best solution, including biomass burning OA (BBOA), hydrocarbon-like OA (HOA), BBOA mixed with cooking-related OA (COA) (biofuel–OA), less-oxidized oxygenated OA (LO-OOA), and more-oxidized oxygenated OA (MO-OOA) (Fig. S4).

At the GIG site, unconstrained PMF (factor 1–8 with fpeak varied from -1 to 1) was also first performed on the OA measured by the ToF–ACSM (Fig. S2). However, we didn't find the best solution due to the ambiguous factor3 (mixed with BBOA and COA) in the 5 factor-solution as shown in Fig. S2. For UMR spectrum, multiple studies show that the BBOA and COA is hard to separate with unconstrained-PMF (Zhang et al., 2019b). Especially, when the BBOA contribution is

less than 10%, their good separation in the unconstrained-PMF is unachievable. However, we know that the Guangzhou sampling site (GIG site) was impacted by the biomass burning from surrounding areas based the results from previous study (Cai et al., 2023; Jiang et al., 2021; Jiang et al., 2022). In addition, in Fig. 1 we show fire spots data during our observation period. The back trajectory data indicates our observation site might impacted by the fire plumes from surrounding. To resolve out the contribution of BBOA, Multilinear Engine 2 (ME-2; SoFi 6.8) (Canonaco et al., 2013) was applied here. Previous study proved that using the standard BBOA spectrum, the BBOA can be efficiently resolved out in the UMR dataset (Crippa et al., 2014; Lanz et al., 2007). We constrained BBOA by applying the standard BBOA mass spectra (Hu et al., 2016; Hu et al., 2013) with a wide range of a value (e.g., a value = 0–1) . Finally, we selected an optimum solution of 5 factors in ME-2 with a value=0 (Figs. S3 and S4), including COA, BBOA, HOA, LO-OOA, and MO-OOA.

Biomass burning OA (BBOA) and Biofuel–OA

The BBOA component was identified at the YBJ site with an obvious peak at m/z 60 ($C_2H_4O_2^+$) and 73 ($C_3H_5O_2^+$) signals in the MS (Fig. S4), which are usually considered as a recognized tracer emitted from biomass burning (Alfarra et al., 2007). Different from the BBOA factor in other cities in eastern China, which is mainly from burning of residual straw or wood for heating, the BBOA in Tibet was mainly from wormwood, cypress branches, highland barley, yak butter, zanba, and so on (Cui et al., 2018; Zhang et al., 2020b). The diurnal variation in BBOA therefore (Fig. S4) showed a unique diurnal pattern with two peaks in the morning (~ 8:00) and evening (20:00–21:00). This pattern was mainly related to the lifecycle of residents in Tibet, who routinely perform “Weisang” activity during the morning and evening each day. The BBOA component identified at GIG site showed different diurnal variation with enhanced afternoon and nighttime peaks likely reflect regional transport of biomass burning emissions from agricultural activities in the Pearl River Delta region during summer (Cai et al., 2023; Wang et al., 2017).

The Biofuel-OA component at the YBJ site was characterized by the highest m/z 55 ($C_3H_3O^+$) signal and a higher ratio of m/z 55/57 compared with HOA (Zhang et al., 2011), as well as the m/z 73 ($C_3H_5O_2^+$) signal. The time series of biofuel-OA component showed a close correlation with emissions of tracking ions fragments $C_3H_3O^+$ (R=0.8) and $C_6H_{10}O^+$ (R=0.93) (Fig. S6), which were also highly correlated with the emissions of biomass burning fragments $C_2H_4O_2^+$ (R=0.93). These findings demonstrated that this factor was associated with emissions of biomass burning and cooking. In this study at YBJ site, the diurnal variation in COA showed three notable peaks corresponding to breakfast time (8:00), lunchtime (13:00), and dinner time (21:00) in Tibet, while peaks occurred at 7:00, 12:00 and 19:00 for GIG site, which coincided with different schedules between urban Guangzhou and remote Tibet.

Hydrocarbon-like OA (HOA)

The HOA component identified at the YBJ site, sourced from traffic emissions and/or other fossil fuel burning activities, presented a high-resolution mass spectrum (Fig. S4) resembling that of former research (Zhang et al., 2011; Ulbrich et al., 2009; Hu et al., 2016; Xu et al., 2014). The hydrocarbon ion series of $C_xH_y^+$ dominated the MS of HOA; therein $C_3H_5^+$, $C_3H_7^+$, $C_4H_7^+$, $C_4H_9^+$, $C_5H_9^+$ and $C_5H_{11}^+$ (m/z = 41, 43, 55, 57, 69, 71) were the main constituents (Ng et al., 2011; Zhang

et al., 2005b; Xu et al., 2014; Zhang et al., 2019a). The O/C ratio of HOA in this study was 0.11, suggesting its fresh property. The tight correlation between HOA versus BC and $C_4H_9^+$ (R = 0.53 and 0.92; Fig. 6a) also indicated that the source of HOA was from traffic emissions. In addition, two distinct peaks of HOA occurred in the morning (8:00-9:00) and evening (20:00-21:00) rush hours (Fig. 4). All these characteristics suggested a reasonable decomposition for HOA. At the GIG site, HOA displayed a bimodal distribution with a moderate morning peak at 07:00 and a stronger evening peak at 20:00 (Fig. 4), consistent with typical urban HOA diurnal patterns. The enhanced evening peak coincides with rush-hour traffic congestion, suggesting intensified vehicular emissions during these periods. Notably, the evening peak magnitude exceeds morning levels, potentially reflecting combined effects of meteorological conditions (e.g., reduced boundary layer height) and emission intensity.

Despite the three POA factors, i.e., HOA, BBOA, and Biofuel OA show similar peak in the morning, their night peaks are different with HOA peaked later an hour than BBOA and Biofuel OA, supporting their different origins based on their time series (e.g., the Pearson correlation coefficient between BBOA and HOA is only 0.41 (Fig. S6a)).

For the POA factors mass spectra, scatter plots showed correlation coefficients between BBOA and HOA, Biofuel-OA and HOA, BBOA and Biofuel-OA were 0.52, 0.85 and 0.64, respectively (Fig. S5), suggesting the BBOA spectra shows distinct differences with HOA and biofuel-OA, however, biofuel-OA and HOA have similarity. Despite the similarity between biofuel-OA and HOA, we can still distinguish them based on their relatively unique and abundant "tracer ions". As shown in Table S2, the most obvious difference between Biofuel-OA and HOA lies in the fact that Biofuel-OA has an obvious higher ratio of m/z 55/57 (2.6) than that of HOA (with m/z 55/57 = 0.9) (Zhang et al., 2011), as well as the higher m/z 60 ($C_2H_4O_2^+$) and 73 ($C_3H_5O_2^+$) signals. Different mass spectra characteristics prove that HOA and biofuel OA have significantly different sources.

Oxygenated OA (OOA)

The mass spectra of MO-OOA and LO-OOA at the YBJ site were characterized by high peaks at m/z 44 (mostly CO_2^+) and LO-OOA had a larger peak at m/z 43 (mostly $C_2H_3O^+$) as well (Crippa et al., 2013; Hu et al., 2016; Lanz et al., 2007; Sun et al., 2010; Zhang et al., 2005a). As a highly oxidizing species, MO-OOA is consistent with the time variation of sulfate (R=0.74; Fig. S6a). Among all OA factors, MO-OOA had the highest O/C (0.78) and the lowest H/C (1.40), indicating a high oxidation degree of this factor, while LO-OOA had the lower O/C (0.55). There is a good correlation between the LO-OOA factor time series and the characteristic ion fragments $C_2H_3O^+$ and $C_3H_3O^+$ with R of 0.95 and 0.75 (Fig. S6a), respectively. The diurnal variation of LO-OOA and MO-OOA was characterized by high values during the day and low values at night, with the fact that MO-OOA concentrations (6:00) increased approximately two hours later than LO-OOA (8:00) during the daytime, indicating different degrees of photochemical aging of local or regional aerosols under strong solar radiation. At the GIG site, the mass spectrum of the MO-OOA was similar to the MO-OOA of the YBJ site, with high peaks at m/z 44 and the diurnal pattern, demonstrating that MO-OOA was significantly influenced by aging processes, in particular photochemistry. The concentration of MO-OOA showed a better correlation with that of sulfate (R = 0.87) than with

nitrate (R = 0.7) (Fig. S6b), which is likely attributed to similarly high oxidation degrees of both MO-OOA and sulfate. The LO-OOA component identified at the GIG site is also characterized by a high m/z 44 signal but lower than that of MO-OOA, indicating its relatively fresh Features.

S2. Uncertainty analysis for the MLR method

Before the MLR method was applied, the correlations between the BrC absorption coefficients at 370nm ($Abs_{BrC,370nm}$) and the mass loadings of OA factors were evaluated as shown in Fig. S10. Results show that BBOA and HOA concentrations were well correlated with $Abs_{BrC,370nm}$ (R = 0.77 and R = 0.64). A moderate correlation (R = 0.31) was also found between $Abs_{BrC,370nm}$ and the LO-OOA mass concentration. The correlation for MO-OOA was near zero, indicating that aging may have reduced the absorption capacity. In addition, the correlation coefficient of each PMF factor was also performed for each campaign. At the YBJ site, it shows that the BBOA factor correlated strongly with the biofuel-OA factor (R = 0.89; Fig. S6a), which caused multicollinearity issues. To solve this issue, we set four different cases via combining or removing the latent collinearity factors to test the sensitivity of the MLR method, including considering all five individual factors (case 1), removing biofuel-OA (case 2), combining BBOA and biofuel-OA (case 3), and removing BBOA (case 4), as shown in Table S5.

At the GIG site, due to the strong similarity among time series of each factor (while different mass spectral profiles as shown in Fig. S4), the factors, except HOA, showed varying degrees of strong correlation with each other, as shown in Fig. S6b. And all OA factors were well or moderately correlated with $Abs_{BrC,370nm}$ (Fig. S10). Based on these problems, we set up three scenarios to test the sensitivity of the MLR method, including considering all five individual factors (case 1) and combining all collinearity factors except HOA (case 2). In addition, we also consider the hypothesis that only BBOA and HOA are absorptive (case 3).

To get the best final solution, we calculated the total uncertainty of the MLR regression coefficients (i.e., MAC) for each case using Monte Carlo. For the Monte Carlo calculation input, the uncertainty of the PMF factor mass concentration needs to be evaluated. A bootstrap analysis (100 iterations; (Ulbrich et al., 2009) was applied, which shows a 9–36 % uncertainty for the PMF factors at the YBJ site and 3 – 9 % at the GIG site, as shown in Table S6. The uncertainty for the coefficient of BrC at 370 nm calculated using $AAE_{BC} = 1$ was estimated to be 43 % for the YBJ site and 36 % for the GIG site based on the lower (0.8) and upper limit of (1.2) previously reported AAE_{BC} range. The total uncertainties of each coefficient for each PMF factor were then calculated by Monte Carlo with 10,000 simulations.

Monte Carlo results show a high total uncertainty (Table S7) of the factors when we don't deal with collinearity at all (i.e., case 1) at both sites, indicating that the collinearity problem among the factors does increase the uncertainty of the MLR regression coefficients (i.e., MAC).
Combining or removing collinearity factors (i.e., case 2–4 for the YBJ site or case 2–3 for the GIG site) can effectively reduce the uncertainty.

Considering that biomass burning is widely reported as an important source of BrC light absorption and regarded as a warming agent affecting global climate (Wang et al., 2025), we

consider all biomass burning related contributing sources when run the MLR model in the case of eliminating the collinearity problemin in this study. As previously reported in the literature (Kasthuriarachchi et al., 2020; Qin et al., 2018), the MAC of COA is nearly zero. Thus, the absorption of light by COA was not considered in this study. For the YBJ site, we finally combined the BBOA factor and the biofuel-OA factor as BBOA (case3). The final results show an uncertainty of BBOA (26.4 %), HOA (20.8 %), LO–OOA (56.3 %), and MO-OOA (57.9%), as shown in Table S7. For the GIG site, we consider only including BBOA and HOA as input variables (case 3) for MLR at the GIG site. And the final results show an uncertainty of HOA (5.8 %), BBOA (6.8 %), and intercept (21.6 %).

We also evaluate the lower and upper limits of the proportion of different sources contributing to the BrC light absorption under all case scenarios. At the YBJ site, the lower limit of MAC is 1.11, 2.04. 0.07 and 0.07 $m^2 g^{-1}$ for BBOA, HOA, LO–OOA, and MO–OOA, while the upper limit of MAC is 2.54, 2.36, 0.23, and 0.29 $m^2 g^{-1}$ for BBOA, HOA, LO–OOA, and MO–OOA. At the GIG site, the lower limit of MAC is 1.91 and 2.57 $m^2 g^{-1}$ for BBOA and HOA, while the upper limit is 2.63 and 0.16 $m^2 g^{-1}$ for HOA and BBOA+LO–OOA+MO–OOA. As shown in Fig. S9, at the YBJ site, BBOA was the significant contributor to BrC light absorption (46 %–54 %), followed by HOA (26 %–43 %) and SOA (11 %–20 %). At the GIG site, HOA was the significant contributor to BrC light absorption (50–54 %), followed by BBOA (36 %) and SOA (0–33 %). Regardless of the case, BBOA is still the dominant absorption contributor at the YBJ site, while HOA is the dominant absorption contributor at the GIG site, as well as the dominant contribution of POA to BrC light absorption in both sites, indicating the robust conclusion in this study.

Table S1. Descriptions of PMF solutions obtained at YBJ site and GIG site.

Factor number	**Fpeak**	**Q/Q_{exp}**	**Solution Description from Free PMF (YBJ site)**
1-3	0	1.4 to 0.93	Too few factors, large residuals at time periods and key m/z's. Q/Q_{exp} decreases very fast.
4	0	0.9	Except MO-OOA, LO-OOA and HOA, the characteristics of one factor is not clear. It seems that BBOA mixed with Biofuel OA.
5	**0**	**0.82**	**Optimum choices for PMF factors (MO-OOA, LO-OOA, HOA, BBOA and Biofuel OA). Time series and diurnal variations of PMF factors are consistent with the external tracers. The spectra of 5 factors are consistent with the source spectra in AMS spectra database.**
6	0	0.8	showed over-split factors without an explicit physical meaning
5	-1 to 1	0.873 to 0.892	Under the 5-factor solution, the factor contributions obtained by different fpeak are relatively stable, clarifying the stability and interpretability of the five-factor solution.
Factor number	**Fpeak/ a value**	**Q/Q_{exp}**	**Solution Description from free PMF and ME2 (GIG site)**
1-3	0	1.96-1.21	Too few factors, large residuals at time periods and key m/z's. Q/Q_{exp} decreases very fast.
4	0	1.15	Too few factors. Factors are mixed based on the time series and spectra.
5	0	1.1	Relatively reasonable profiles and time series under a fully unconstrained condition. However, BBOA was still mixed in other factors.
6	0	1.01	Factor split, e.g., COA was split into two factors with similar spectra, however, different time series.
5	-1 to 1	1.104 to 1.112	Under the 5-factor solution, factor MS and time series are nearly identical and the factor contributions obtained by different fpeaks are relatively stable, clarifying the stability and interpretability of the five-factor solution.
Factor number	**a value**	**Q/Q_{exp}**	**Solution Description from ME2 (GIG site)**
5	**a value: 0**	**1.05**	**Optimum choices for PMF factors (MO-OOA, LO-OOA, HOA, BBOA and COA) resolved by ME2. Time series and diurnal variations of PMF factors are consistent with the external tracers. The spectra of 5 factors are consistent with the source spectra in AMS spectra database.**
5	a value: 0 to 0.8	1.03 to 1.05	Under the 5-factor solution, factor MS and time series are nearly identical under different a value (Fig. S3)

Table S2. The main mass spectra characteristics of PMF factors at YBJ site and GIG site.

Factor	Main mass spectra characteristics (YBJ site)
HOA	dominated by alkyl fragments ($C_nH_{2n+1}^+$ and $C_nH_{2n-1}^+$). The O/C ratio of HOA in this study was 0.11, suggesting its fresh property. The tight correlation between HOA versus BC and $C_4H_9^+$ (R = 0.53 and 0.92; Fig. S6a) also indicated that the source of HOA was from traffic emissions.
BBOA	characterized by an obvious peak at m/z 60 ($C_2H_4O_2^+$) and 73 ($C_3H_5O_2^+$) signals in the MS (Fig. S4), which are usually considered as a recognized tracer emitted from biomass burning.
Biofuel OA	characterized by the highest m/z 55 ($C_3H_3O^+$) signal and a higher ratio of m/z 55/57 (2.6) compared with HOA (0.9) (Zhang et al., 2011), as well as the m/z 73 ($C_3H_5O_2^+$) signal. The time series of biofuel OA component showed a close correlation with emissions of tracking ions fragments $C_3H_3O^+$ (R=0.8) and $C_6H_{10}O^+$ (R=0.93) (Fig. S6), which were also highly correlated with the emissions of biomass burning fragments $C_2H_4O_2^+$ (R=0.93). These findings demonstrated that this factor was associated with emissions of biomass burning and cooking.
LO-OOA	characterized by high peaks at m/z 44 (mostly CO_2^+) and had a larger peak at m/z 43 (mostly $C_2H_3O^+$) than MO-OOA as well. LO-OOA had a lower O/C (0.55) than MO-OOA. There is a good correlation between the LO-OOA factor time series and the characteristic ion fragments $C_2H_3O^+$ and $C_3H_3O^+$ with R of 0.95 and 0.75 (Fig. S6a), respectively.
MO-OOA	characterized by high peaks at m/z 44 (mostly CO_2^+) and the time series was consistent with sulfate (R=0.74; Fig. S6a). MO-OOA had the highest O/C (0.78) and the lowest H/C (1.40), indicating a high oxidation degree of this factor
Factor	**Mass spectra characteristics (GIG site)**
HOA	dominated by alkyl fragments ($C_nH_{2n+1}^+$ and $C_nH_{2n-1}^+$). HOA displayed a bimodal distribution with a moderate morning peak at 07:00 and a stronger evening peak at 20:00 (Fig. S4), consistent with typical urban HOA diurnal patterns.
BBOA	characterized by an obvious peak at m/z 60 and 73 signals and showed different diurnal variation with enhanced afternoon and nighttime peaks likely reflect regional transport of biomass burning emissions from agricultural activities in the Pearl River Delta region during summer.
COA	characterized by the highest m/z 55 signal and a higher ratio of m/z 55/57 compared with HOA. The diurnal variation showed three notable peaks (7:00, 12:00 and 19:00), corresponding to breakfast time, lunchtime, and dinner time.
LO-OOA	characterized by a high m/z 44 signal but lower than that of MO-OOA, indicating its relatively fresh features.
MO-OOA	characterized by high peaks at m/z 44. The concentration of MO-OOA showed a better correlation with that of sulfate (R = 0.87) than with nitrate (R = 0.7) (Fig. S6b), which is likely attributed to similarly high oxidation degrees of both MO-OOA and sulfate.

Table S3. The AAE_{BC} values used to separate BC and BrC light absorption in other studies.

Observation sites	AAE_{BC}	Reference
Qomolangma Station	1.187	(Zhang et al., 2021b)
Nam Co Station	1.086	
Waliguan Station	1.042	
Lhasa	1	(Zhu et al., 2017)
Lulang	1	
Gaomeigu	1.1	(Tian et al., 2023)
Xianghe	1.1	(Wang et al., 2019)
Beijing 2016	1	(Xie et al., 2019)
Beijing 2020	1	(Sun et al., 2021)
Gucheng	1	
Xian	1	(Zhang et al., 2020a)
Hong Kong	1	
Singapore	0.99 to 1.04	(Kasthuriarachchi et al., 2020)

Table S4. The summary of BrC light absorption coefficients and the contributions at 370 nm, as well as the OA mass concentration and primary OA fraction, are based on the literature results. The results were categorized according to the locations of their observation sites (Arctic region, Qinghai–Tibet Plateau (QTP region), Southern China, and Northern China).

Sites	$Fraction_{BrC}$ (%)	Abs_{BrC} (M m^{-1})	OA (μg m^{-3})	$Fraction_{POA}$ (%)	References
Arctic region					
circum–Arctic		0.1			(Yue et al., 2022)
Alert		0.04			(Yue et al., 2019)
Utqiagvik, Alaska		0.2			(Barrett and Sheesley, 2017)
QTP region					
Lhasa (Autumn)	8	4.2			(Zhu et al., 2017)
Beiluhe (Summer)	12.0	1.6			(Zhu et al., 2021)
Beiluhe (Autumn)	15.2	2.4			(Zhu et al., 2021)
YBJ site (Summer; **This study**)	15.4	0.2	0.7	34	
Beiluhe (Spring)	16.2	1.9			(Zhu et al., 2021)
Beiluhe (1 year)	18.0	2.0			(Zhu et al., 2021)
NamCo (Spring+Summer)	21.3	0.7			(Zhang et al., 2021b)
WLG(Summer)	22.4	0.6			(Zhang et al., 2021b)
Beiluhe (winter)	25.9	2.1			(Zhu et al., 2021)
Ngari (Autumn)	27.4	7.6			(Zhu et al., 2021)
Ngari (Summer)	31.4	5.9			(Zhu et al., 2021)
Lulang (Autumn)	32.0	4.8			(Zhu et al., 2017)
QOMS (Spring)	33.1	4.4	2.4	86	(Zhang et al., 2021b)
Qinghai Lake (Summer)	33.9	4.1			(Zhu et al., 2021)
Ngari (one year)	35.0	7.3			(Zhu et al., 2021)
Ngari (Spring)	36.7	6.1			(Zhu et al., 2021)
Gaomeigu (Spring)	37.0	12.3			(Tian et al., 2023)
Qinghai Lake (Spring)	38.6	9.3			(Zhu et al., 2021)
Ngari (winter)	40.7	10.7			(Zhu et al., 2021)
Qinghai Lake (winter)	43.0	9.6			(Zhu et al., 2021)
Qinghai Lake (1 year)	44.0	9.1			(Zhu et al., 2021)

Qinghai Lake (Autumn)	54.4	14.9			(Zhu et al., 2021)
Southern China					
Hong Kong (Winter)	11.0	6.3			(Zhang et al., 2020a)
Nanjing (Summer)	14.4	26.5			(Bao et al., 2022)
Nanjing (Spring)	16.1	29.7			(Bao et al., 2022)
Nanjing (3 years)	16.7	6.3			(Wang et al., 2018)
Nanjing (Autumn)	17.0	37.3			(Bao et al., 2022)
Nanjing (Winter)	19.6	51			(Bao et al., 2022)
GIG site (Summer; **This study**)	21.0	2.9	6.9	29	
Guangzhou, Panyu (Winter)	23.6	13.7	20	40	(Qin et al., 2018)
Wuhan (Winter)	28.7				(Zhang et al., 2021a)
Northern China					
Xian (Winter, Normal)	29.0	49.4	43.3	49	(Zhang et al., 2022)
Beijing (Winter 2020)	36.0	24	11.25	56.3	(Sun et al., 2021)
Shanghai (Winter)	37.6				(Zhang et al., 2021a)
Gucheng (Winter)	38.0	66.5	21.33	51.2	(Sun et al., 2021)
Harbin (Winter)	40.6				(Zhang et al., 2021a)
Beijing (Winter 2016)	46.0			77	(Xie et al., 2019)
Xian (Winter, Lockdown)	49.0	47.7	29.4	44	(Zhang et al., 2022)
Xianghe (Winter)	58.0	61.8			(Wang et al., 2019)

Table S5. Regression coefficients (MAC) of the multiple linear regression (MLR) at 370,470, 520, 590, and 660 nm at the YBJ site and GIG site.

YBJ site

		Wavelength (nm)				
		370nm	470nm	520nm	590nm	660nm
Case1	BBOA	2.54±0.53	0.66±0.25	0.25±0.18	0.11±0.11	0±0.13
	HOA	2.36±0.31	1.16±0.14	0.20±0.1	0.16±0.06	0±0.08
	LO–OOA	0.07±0.08	0.13±0.04	0.06±0.03	0.04±0.02	0±0.02
	MO–OOA	0.29±0.19	0.20±0.09	0±0.06	0.02±0.04	0±0.05
	biofuel–OA	0±0.42	0.22±0.20	0±0.14	0.10±0.09	0±0.1
	intercept	0±0.02	0.02±0.01	0.04±0.01	0.02±0	0.03±0
Case2	biofuel–OA	1.80±0.19	0.70±0.09	0.18±0.06	0.18±0.04	0±0.04
	HOA	2.04±0.32	1.08±0.14	0.17±0.1	0.15±0.06	0±0.07
	LO–OOA	0.23±0.08	0.17±0.03	0.08±0.02	0.05±0.01	0.01±0.02
	MO–OOA	0.07±0.19	0.15±0.09	0±0.06	0.01±0.04	0±0.04
	intercept	0±0.02	0.02±0.01	0.04±0.01	0.02±0	0.03±0
Case3	BBOA+ biofuel–OA	1.11±0.11	0.42±0.05	0.11±0.03	0.11±0.02	0±0.03
	HOA	2.08±0.30	1.11±0.14	0.18±0.1	0.16±0.06	0±0.07
	LO–OOA	0.15±0.08	0.14±0.03	0.07±0.02	0.04±0.02	0.01±0.02
	MO–OOA	0.18±0.18	0.19±0.08	0±0.06	0.02±0.04	0±0.04
	intercept	0±0.02	0.02±0.01	0.04±0.01	0.02±0	0.03±0
Case4	BBOA	2.54±0.23	0.92±0.11	0.25±0.08	0.23±0.05	0±0.06
	HOA	2.36±0.28	1.24±0.13	0.20±0.09	0.20±0.06	0±0.07
	LO–OOA	0.07±0.08	0.12±0.04	0.06±0.03	0.04±0.02	0±0.02
	MO–OOA	0.29±0.18	0.22±0.09	0±0.06	0.03±0.04	0±0.04
	intercept	0±0.02	0.02±0.01	0.04±0.01	0.02±0	0.03±0

GIG site

		Wavelength (nm)				
		370nm	470nm	520nm	590nm	660nm
Case1	COA	0.78±0.39	0.17±0.19	0.05±0.11	0.04±0.08	0±0.04
	BBOA	0±3.23	0±1.51	0±0.87	0±0.63	0±0.31
	HOA	1.67±0.48	1.32±0.24	0.72±0.14	0.40±0.1	0.17±0.05
	LO–OOA	0±0.35	0±0.17	0±0.09	0±0.07	0±0.03
	MO–OOA	0.19±0.34	0.11±0.16	0.04±0.07	0.05±0.07	0.03±0.03
	intercept	0.57±0.19	0.22±0.09	0.43±0.05	0.17±0.04	0.11±0.02
Case2	HOA	2.93±0.27	1.57±0.12	0.79±0.07	0.45±0.05	0.16±0.03
	BBOA+LO–OOA+MO–OOA	0.16±0.02	0.08±0.01	0.03±0	0.03±0	0.02±0
	intercept	0.34±0.17	0.17±0.08	0.41±0.05	0.16±0.03	0.11±0.02
Case3	HOA	2.57±0.28	1.40±0.13	0.72±0.07	0.38±0.06	0.13±0.03
	BBOA	1.91±0.21	0.90±0.10	0.35±0.06	0.40±0.04	0.20±0.02
	intercept	0.37±0.17	0.18±0.08	0.42±0.04	0.17±0.03	0.11±0.02

Table S6. Quantitative assessment of the uncertainty of the PMF factors was made by bootstrapping analysis with 100 iterations.

YBJ site	Uncertainty	GIG site	Uncertainty
BBOA	23%	BBOA	5%
HOA	36%	HOA	4%
biofuel–OA	23%	COA	4%
LO–OOA	9%	MO–OOA	3%
MO–OOA	15%	LO–OOA	5%
BBOA+ biofuel–OA	33%	BBOA+MO–OOA+LO–OOA	8%
$Abs_{BrC,370nm}$	43%	$Abs_{BrC,370nm}$	36%

Table S7. The uncertainty of multiple linear regression (MLR) at 370 nm using Monte Carlo simulations at the YBJ site and GIG site.

YBJ site

CASE		Mean	Standard deviation	Uncertainty (%) (100*std/mean)
Case1	BBOA	2.06	0.81	39.3
	HOA	2.07	0.39	19.0
	LO–OOA	0.10	0.09	88.1
	MO–OOA	0.27	0.11	42.7
	biofuel–OA	0.43	0.49	114.3
	intercept	0	0	
Case2	biofuel–OA	1.78	0.43	24.2
	HOA	1.91	0.42	22.0
	LO–OOA	0.22	0.07	33.2
	MO–OOA	0.11	0.09	83.5
	intercept	0	0	
Case3	BBOA+ biofuel–OA	1.06	0.28	26.4
	HOA	2.02	0.42	20.8
	LO–OOA	0.16	0.09	56.2
	MO–OOA	0.19	0.11	57.9
	intercept	0	0	
Case4	BBOA	2.55	0.60	23.4
	HOA	2.22	0.37	16.7
	LO–OOA	0.09	0.09	97.2
	MO–OOA	0.29	0.11	37.6
	intercept	0	0	

GIG site

CASE		Mean	Standard deviation	Uncertainty (%) (100*std/mean)
Case1	COA	0.74	0.14	19.5
	BBOA	0.23	0.49	216.4
	MO–OOA	0.16	0.06	37.5
	HOA	1.72	0.26	15.1
	LO–OOA	0.00	0.02	552.3
	intercept	0.57	0.08	14.8
Case2	BBOA+MO–OOA+LO–OOA	0.16	0.01	6.2
	HOA	2.98	0.18	6.0
	intercept	0.35	0.08	23.5
Case3	BBOA	1.87	0.11	5.8
	HOA	2.62	0.18	6.8
	intercept	0.38	0.08	21.6

Table S8. The summary of campaign–averaged light absorption coefficients (M m^{-1}) of total aerosols, BC, and BrC, as well as the BrC contribution to the total absorption of particles (f_{BrC}, %).

Average ± SD		370nm	470nm	520nm	590nm	660nm	880nm
YBJ	Total	1.59±1.59	1.19±1.24	1.01± 1.05	0.88± 0.92	0.76±0.80	0.58±0.60
	BC	1.34±1.46	1.06±1.15	0.96±1.04	0.84±0.92	0.75±0.82	0.58±0.60
	BrC	0.22±0.32	0.13±0.17	0.05±0.08	0.03± 0.05	0.02±0.03	0
	f_{BrC}	15.4±14.0	13.0±13.2	8.5±13.4	6.4±11.5	5.2±11.8	0
GIG	Total	13.2±7.0	9.5±5.1	8.1±4.4	7.1±3.7	6.1±3.3	4.4±2.4
	BC	10.5±5.6	8.3±4.4	7.5±4.0	6.6±3.5	5.9±3.1	4.4±2.4
	BrC	2.9±2.0	1.5±0.9	1.1±0.5	0.6± 0.4	0.3± 0.2	0
	f_{BrC}	21.0±7.8	14.9±6.2	12.5±7.8	8.5±4.3	5.1±3.4	0

Table S9. The summary of OA factors contributing to BrC absorption at 370 nm using the PMF–MLR method. The asterisks (*) represent the absorption contributions of soluble BrC from different sources at 365nm. The sources include POA (primary OA) (BBOA (biomass burning OA), HOA (hydrocarbon–like OA), CCOA (coal combustion OA), COA (cooking–related OA), NOA (nitrogen-containing OA); If other types of BrC primary sources exist in the literature, they are unified as POA and SOA (secondary OA).

Sites	BBOA	HOA	CCOA	COA	NOA	*POA	*SOA*	Unidentified	References
China									
Gucheng (winter)	(16%)	(10%)	(42%)				(52%)		(Sun et al., 2021)
Beijing (winter 2016)	(17%)		(48%)	(3%)			(32%)		(Xie et al., 2019)
Beijing (winter 2020)			(56%)	(7%)			(37%)		(Sun et al., 2021)
Xianghe (winter)	(49%)	(4%)	(28%)				(19%)		(Wang et al., 2019)
$Xian_{lockdown}$ (winter)	(20%)	(11%)	(28%)				(40%)	(1%)	(Zhang et al., 2022)
$Xian_{normal}$ (winter)	(17%)	(20%)	(45%)				LO–OOA (12%)	(6%)	
Guangzhou(summer; **This study**)	(36%)	(51%)						(13%)	
Guangzhou (Winter 2014)	(25%)	(23%)					LV–OOA (52%)		(Qin et al., 2018)
QTP region									
Gaomeigu (Spring)	(51%)						po–OOA (49%)		(Tian et al., 2023)
QOMS (Spring)	(64%)				(20%)		MO–OOA (16%)		(Zhang et al., 2021b)
YBJ (Summer; **This study**)	(40%)	(38%)					(22%)		
Other countries									
Paris (winter)	(74%)	(8%)					OOA (18%)		(Zhang et al., 2020c)
Delhi (winter)	(48%)	(10%)					SV–OOA (26%)	(16%)	(Singh et al., 2021)
Athens (winter)	(33%)	(13%)		(13%)			(41%)		(Kaskaoutis et al., 2021)
Singapore (winter)		(83%)		(2%)			LO–OOA (15%)		(Kasthuriarachchi et al., 2020)
Manaus (Summer+Autumn)	(57%)	(22%)					(17%)	(4%)	(De Sá et al., 2019)
Mexico (winter)	(14%)	(54%)					(24%)		
Mexico (Spring)	(55%)	(40%)					(0.2%)	(4.8%)	(Retama et al., 2022)
Mexico (Summer)	(6%)	(49%)					(5%)	(40%)	
Mexico (Winter to summer)	(43%)	(46%)					(6%)	(5%)	
***Soluble BrC a 365nm**									
*Central Alabama (Summer)	(85%)						LO–OOA (10%)	(3%)	(Washenfelder et al., 2015)
*Urumqi (Winter)						(46%)	(54%)		
*Xining (Winter)						(51%)	(49%)		(Zhong et al., 2023)
*Lanzhou (Winter)						(60%)	(40%)		
*Yinchuan (Winter)						(30%)	(70%)		
*Xian (Winter)	(19%)	(12%)	(13%)				OOA (28%)	(28%)	(Lei et al., 2019)
*Xian (Summer)		(7%)	(1%)				OOA (75%)	(17%)	
*Yangzhou (Autumn to early Spring)	(24%)	(19%)					(47%)		(Chen et al., 2020)

*Nanjing (Spring)	(58%)	(42%)	(Bao et al., 2022)
*Nanjing (Summer)	(44%)	(56%)	
*Nanjing (Autumn)	(75%)	(25%)	
*Nanjing (Winter)	(60%)	(40%)	

Note:

**Nanjing SOA = anthropogenic SOA+ biogenic SOA + secondary nitrate and sulfate formation*

**Urumqi Xining Lanzhou Yinchuan SOA = HO–OOA1 + HO–OOA2 + LO–OOA*

Mexico SOA = LO–OOA+MO–OOA

**Yangzhou SOA = LO–OOA+MO–OOA*

Paris BBOA = LO–BBOA+MO–BBOA

Manaus BBOA = LO–BBOA+MO–BBOA

Manaus SOA = MO–OOA+LO–OOA+IEPOX–SOA

Athens SOA = SV–OOA+LV–OOA

Singapore HOA = HOA+O–HOA

Beijing CCOA = FFOA

Beijing (winter 2016)–SOA = aqOOA + OPOA+OOA

Beijing (winter 2020)–SOA = LO–OOA+MO–OOA

$Xian_{lockdown}$ SOA = LO–OOA + MO–OOA

Table S10. The literature summary of MAC ($m^2\ g^{-1}$) from different BrC sources, which was obtained by the PMF–MLR method in different environments. All the results were categorized based on the locations of their observation sites (urban China, Qinghai–Tibet Plateau (QTP region), and other countries).

Sites	BBOA	HOA	CCOA	LO–OOA	MO–OOA	References
Urban China						
Xianghe (winter)	3.40±0.16	0.50±0.16	5.73±0.32			(Wang et al., 2019)
Guangzhou (Winter 2014)	3.40±0.41	0.61±0.05			1.04±0.08	(Qin et al., 2018)
$Xian_{normal}$ (winter)	1.66±0.08	1.44±0.08	5.35±0.13	0.71±0.05	–0.26±0.08	(Zhang et al., 2022)
$Xian_{lockdown}$ (winter)	2.39±0.13	1.92±0.19	5.22±0.19	2.08±0.14	0.73±0.14	
Guangzhou (Summer; **This study**)	1.91±0.21	2.57±0.28				
QTP region						
Gaomeigu (Spring)	2.78±0.39				1.43±0.23	(Tian et al., 2023)
QOMS (Spring)	2.29±0.02				0.60±0.03	(Zhang et al., 2021b)
YBJ (Summer; **This study**)	1.11–2.54	2.08±0.30		0.15±0.08	0.18±0.08	
Other countries						
Delhi (winter)	0.86	0.42		0.67		(Singh et al., 2021)
Manaus (Summer+Autumn)	(LO–BBOA) 1.5±0.07 (MO–BBOA) 0.82±0.01	2.04±0.14		0.01±0.02	0.01±0.02	(De Sá et al., 2019)
Athens (winter)	7.63±0.74	1.34±0.49		4.02±0.44	1.98±0.33	(Kaskaoutis et al., 2021)
Paris (winter)	(LOBBOA) 4.86±0.18 (MO–BBOA) 2.02 ±0.12	1.06±0.23		(OOA) 0.55±0.05		(Zhang et al., 2020c)
Central Alabama (Summer)	1.35±0.06			0.03±0.02	–0.01±0.01	(Washenfelder et al., 2015)
Mexico (Spring)	1.82±0.02	1.76±0.03		0.01±0.04	0±0.01	(Retama et al., 2022)
Mexico (Summer)	0.4±0.14	1.47±0.07		0.03±0.06	0.04±0.03	
Mexico (winter)	0.83±0.09	1.79±0.03		0.97±0.06	–0.14±0.02	
Mexico (Winter to summer)	1.73±0.02	1.75±0.02		0.29±0.03	0±0.01	
Singapore (winter)		0.97±0.33		0.67±0.23		(Kasthuriarachchi et al., 2020)

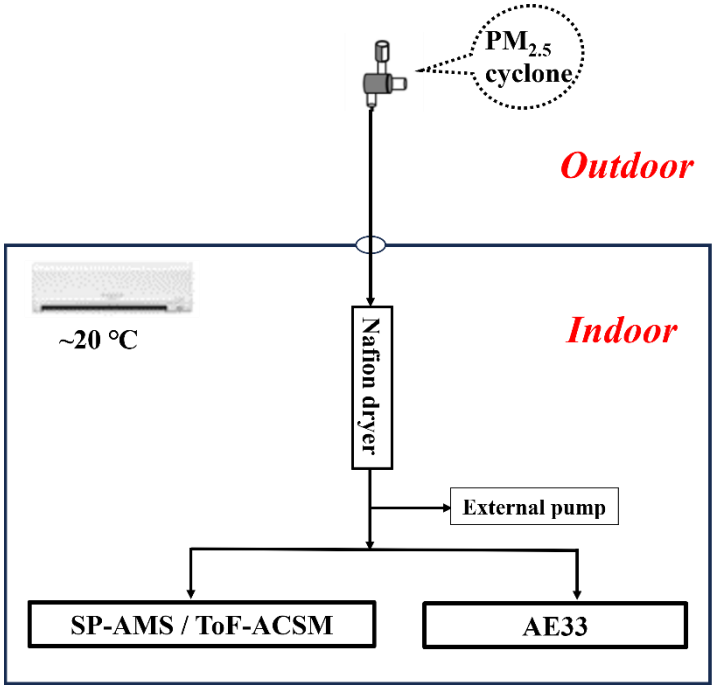

Figure S1. The setup diagram of instruments during campaign in Yangbajing and Guangzhou.

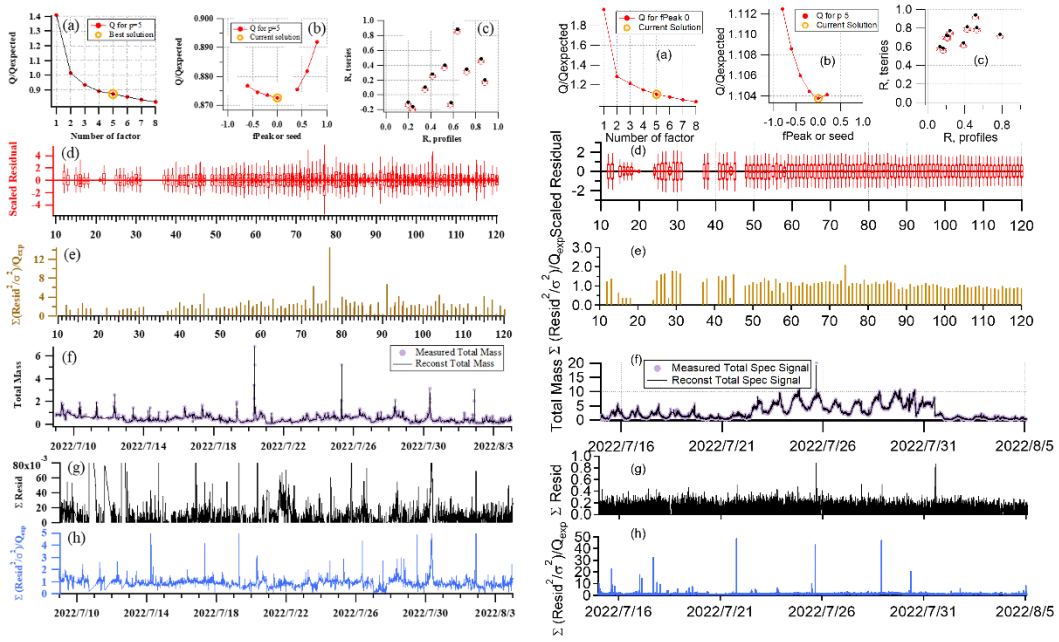

Figure S2. Diagnostics plots of factor selections in the unconstrained PMF at the YBJ site (left) and the GIG site (right).

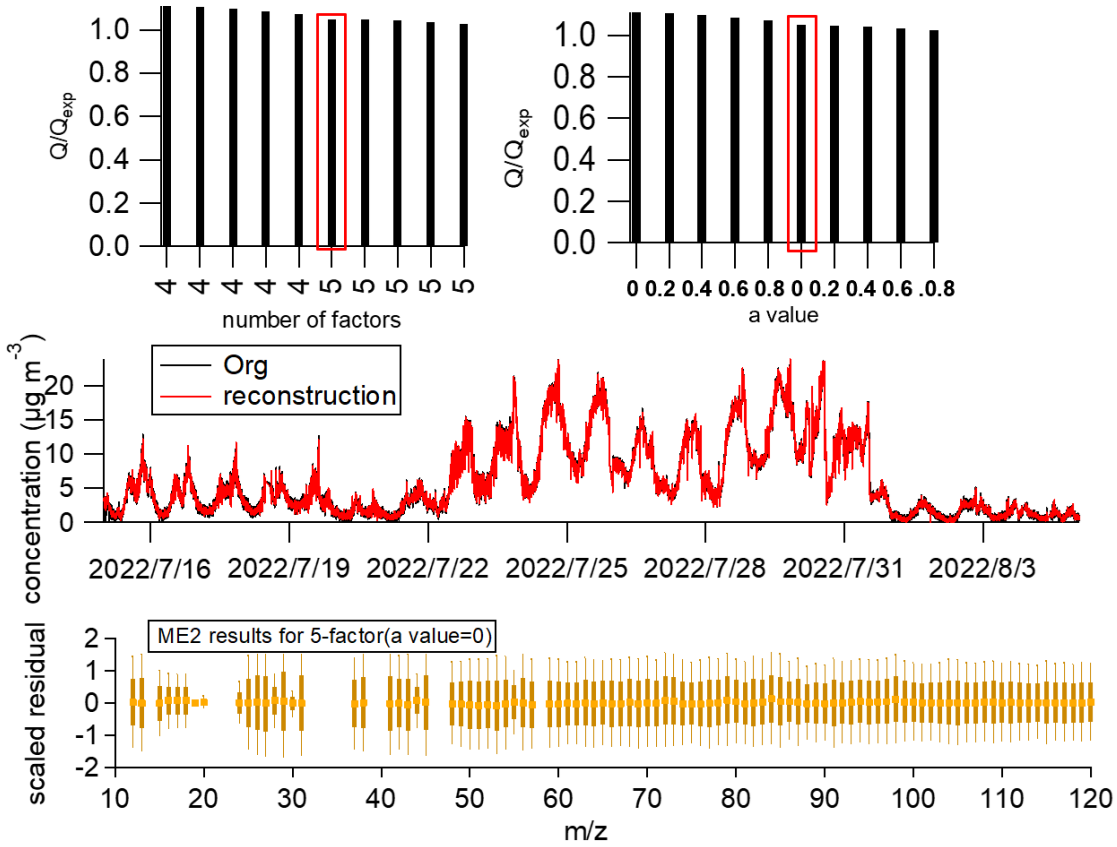

Figure S3. ME2-Diagnostics plots of factor selections at the GIG site.

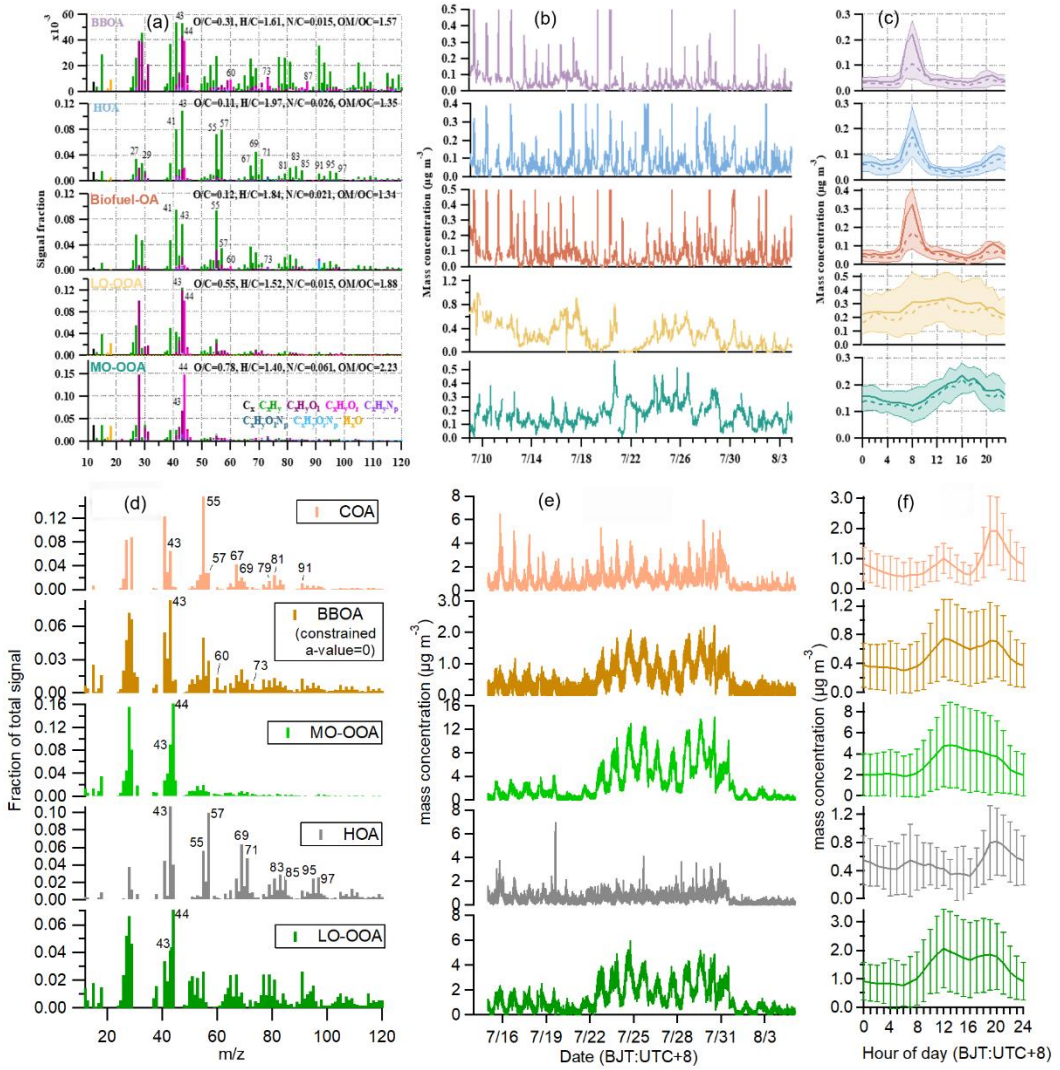

Figure S4. The final optimum solution for OA sources at the YBJ site and the GIG site. The mass spectrum was plotted in the form of UMR, and each peak was colored on the basis of the contributions of 8 ion categories: C_x^+, $C_xH_y^+$, $C_xH_yO_1^+$, $C_xH_yO_z^+$, $C_xH_yN_p^+$, $C_xH_yO_1N_p^+$, $C_xH_yO_zN_p^+$, H_xO^+.

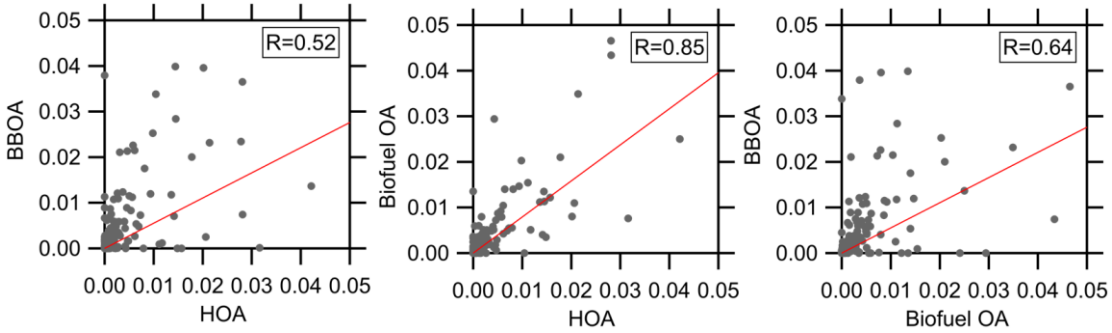

Figure S5. Mass spectra scatter plots among BBOA, HOA and Biofuel-OA at YBJ site.

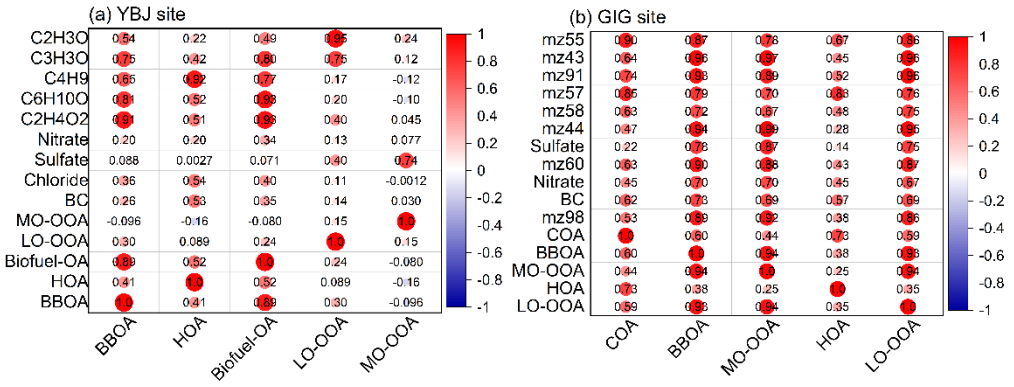

Figure S6. The Pearson's correlation coefficient (R) between the OA factor and tracers at the YBJ site and the GIG site.

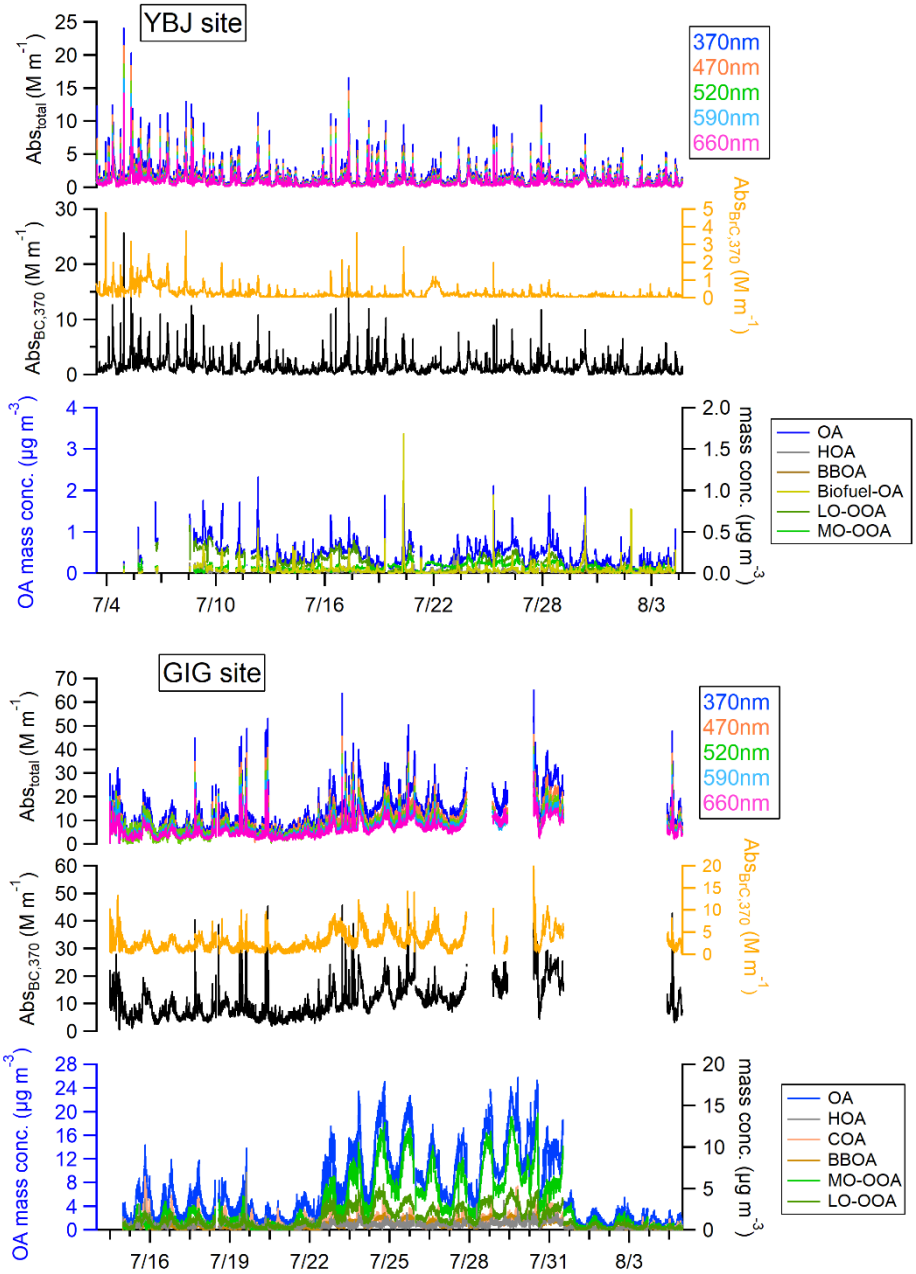

Figure S7. The time series of OA mass concentration and BrC light absorption coefficients at 370, 470, 520, 590, and 660 nm at the YBJ site and GIG site.

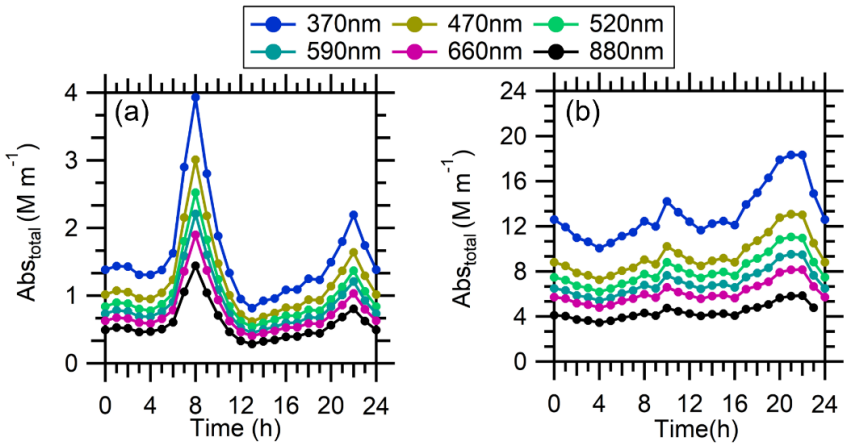

Figure S8. Diurnal variations of light absorption of total aerosol at seven wavelengths at the YBJ site (a) and the GIG site (b).

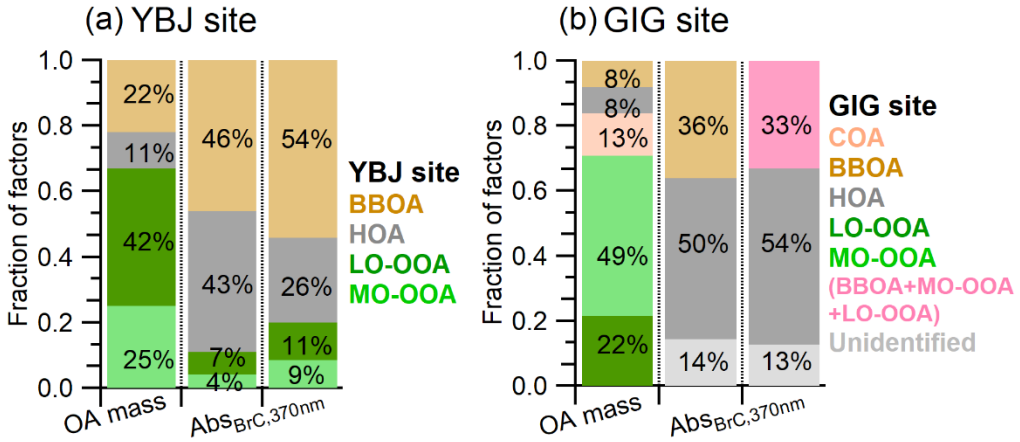

Figure S9. (a) The contributions of different OA factors to total OA (left) and contributions of different OA factors to BrC light absorption at 370 nm (Center and right; represent a upper and lower bound based on the different cases discussed in Section 2.5.1 and Section S2) at YBJ site (a) and GIG site (b).

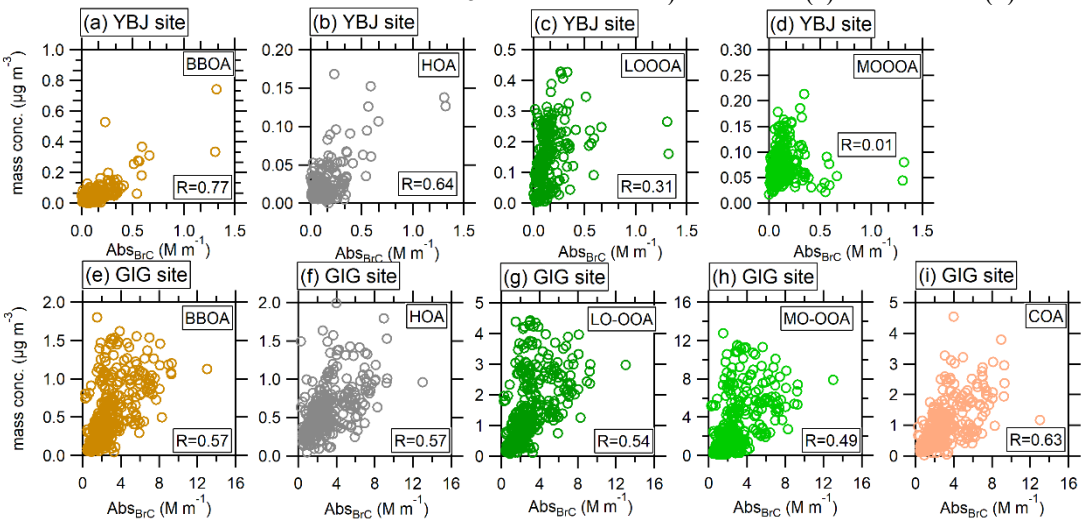

Figure S10. Scatter plots of brown carbon absorption at 370 nm versus the mass concentrations of OA factors during the campaign.

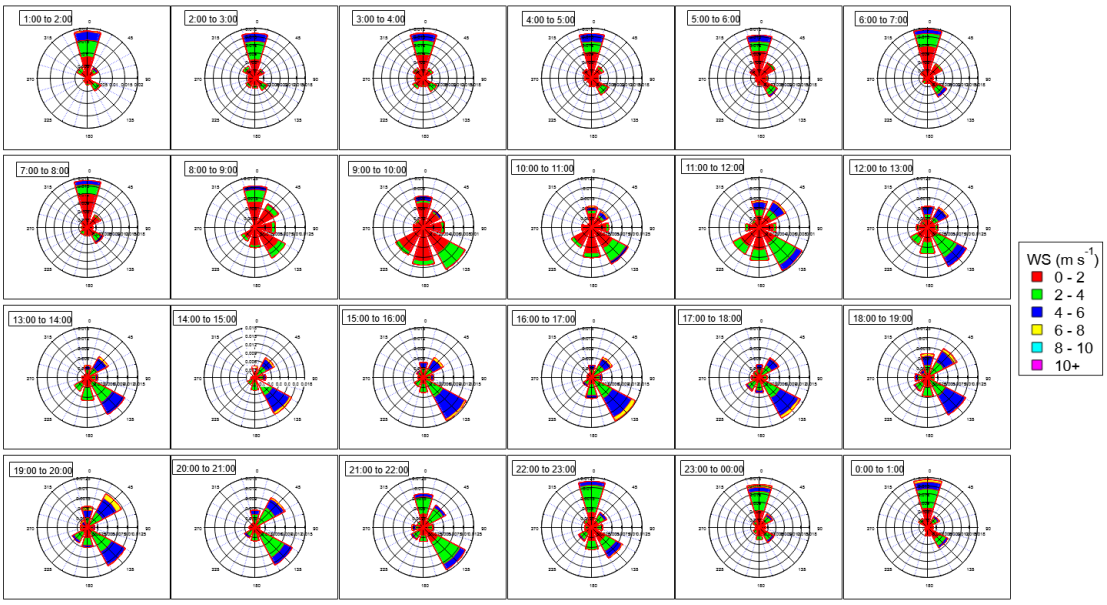

Figure S11. Hourly rose plots at the YBJ site.

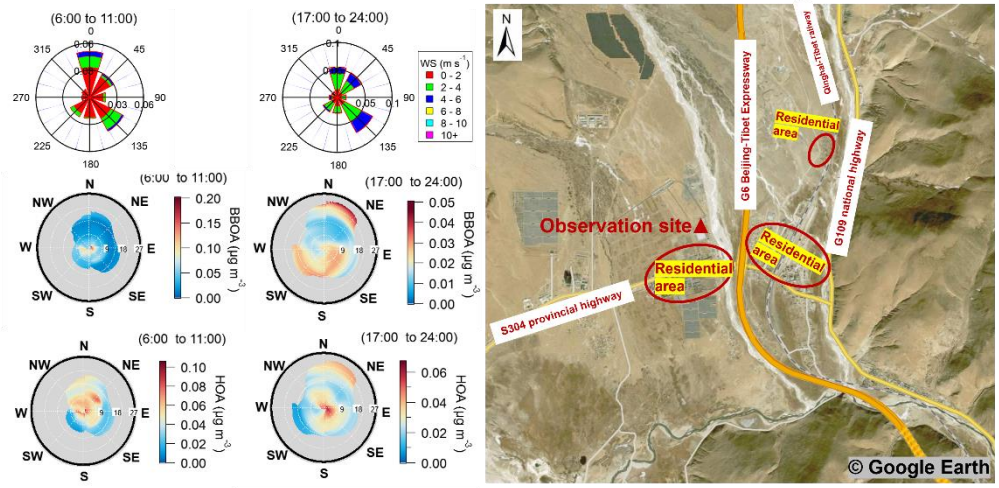

Figure S12. Rose plots and Bivariate polar plots of HOA and BBOA during morning peak (6:00 to 11:00) and evening peak (17:00 to 24:00). The unit of wind speed is km h^{-1} in the Bivariate polar plots. (map source: © Google Earth)

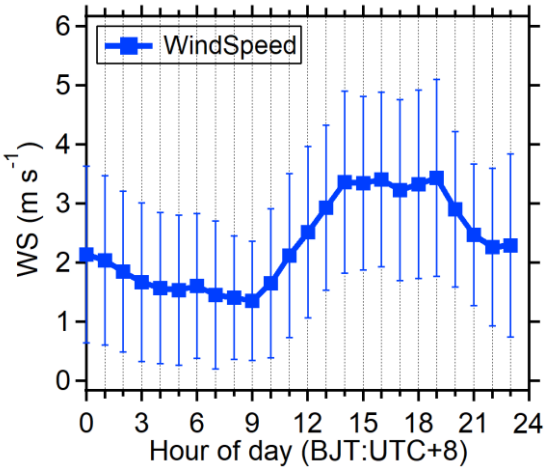

Figure S13. The diurnal variations of wind speed at the YBJ site

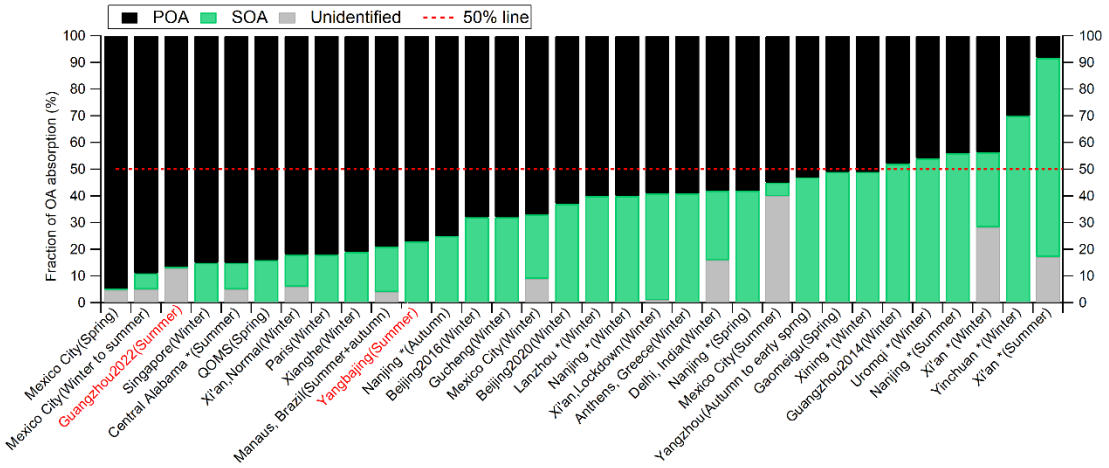

Figure S14. The summary of the contribution of organic aerosols from different sources to BrC absorption at 370 nm using the PMF–MLR method. The asterisks (*) represent the absorption contributions of soluble BrC from different sources at 365nm. The sources include POA (primary OA) and SOA (secondary OA). The dashed line represents 50% of BrC absorption.

Reference

Alfarra, M. R., Prevot, A. S. H., Szidat, S., Sandradewi, J., Weimer, S., Lanz, V. A., Schreiber, D., Mohr, M., and Baltensperger, U.: Identification of the Mass Spectral Signature of Organic Aerosols from Wood Burning Emissions, Environmental Science & Technology, 41, 5770-5777, 10.1021/es062289b, 2007.

Bao, M., Zhang, Y.-L., Cao, F., Lin, Y.-C., Hong, Y., Fan, M., Zhang, Y., Yang, X., and Xie, F.: Light absorption and source apportionment of water soluble humic-like substances (HULIS) in PM2.5 at Nanjing, China, Environmental Research, 206, 10.1016/j.envres.2021.112554, 2022.

Barrett, T. E. and Sheesley, R. J.: Year-round optical properties and source characterization of Arctic organic carbon aerosols on the North Slope Alaska, Journal of Geophysical Research: Atmospheres, 122, 9319-9331, 10.1002/2016jd026194, 2017.

Cai, Y., Ye, C., Chen, W., Hu, W., Song, W., Peng, Y., Huang, S., Qi, J., Wang, S., Wang, C., Wu, C., Wang, Z., Wang, B., Huang, X., He, L., Gligorovski, S., Yuan, B., Shao, M., and Wang, X.: The important contribution of secondary formation and biomass burning to oxidized organic nitrogen (OON) in a polluted urban area: insights from in situ measurements of a chemical ionization mass spectrometer (CIMS), Atmospheric Chemistry and Physics, 23, 8855-8877, 10.5194/acp-23-8855-2023, 2023.

Canonaco, F., Crippa, M., Slowik, J. G., Baltensperger, U., and Prévôt, A. S. H.: SoFi, an IGOR-based interface for the efficient use of the generalized multilinear engine (ME-2) for the source apportionment: ME-2 application to aerosol mass spectrometer data, Atmospheric Measurement Techniques, 6, 3649-3661, 10.5194/amt-6-3649-2013, 2013.

Chen, Y., Xie, X., Shi, Z., Li, Y., Gai, X., Wang, J., Li, H., Wu, Y., Zhao, X., Chen, M., and Ge, X.: Brown carbon in atmospheric fine particles in Yangzhou, China: Light absorption properties and source apportionment, Atmospheric Research, 244, 10.1016/j.atmosres.2020.105028, 2020.

Crippa, M., Decarlo, P. F., Slowik, J. G., Mohr, C., Heringa, M. F., Chirico, R., Poulain, L., Freutel, F., Sciare, J., Cozic, J., Di Marco, C. F., Elsasser, M., Nicolas, J. B., Marchand, N., Abidi, E., Wiedensohler, A., Drewnick, F., Schneider, J., Borrmann, S., Nemitz, E., Zimmermann, R., Jaffrezo, J. L., Prévôt, A. S. H., and Baltensperger, U.: Wintertime aerosol chemical composition and source apportionment of the organic fraction in the metropolitan area of Paris, Atmospheric Chemistry and Physics, 13, 961-981, 10.5194/acp-13-961-2013, 2013.

Crippa, M., Canonaco, F., Lanz, V. A., Äijälä, M., Allan, J. D., Carbone, S., Capes, G., Ceburnis, D., Dall'Osto, M., Day, D. A., DeCarlo, P. F., Ehn, M., Eriksson, A., Freney, E., Hildebrandt Ruiz, L., Hillamo, R., Jimenez, J. L., Junninen, H., Kiendler-Scharr, A., Kortelainen, A. M., Kulmala, M., Laaksonen, A., Mensah, A. A., Mohr, C., Nemitz, E., O'Dowd, C., Ovadnevaite, J., Pandis, S. N., Petäjä, T., Poulain, L., Saarikoski, S., Sellegri, K., Swietlicki, E., Tiitta, P., Worsnop, D. R., Baltensperger, U., and Prévôt, A. S. H.: Organic aerosol components derived from 25 AMS data sets across Europe using a consistent ME-2 based source apportionment approach, Atmospheric Chemistry and Physics, 14, 6159-6176, 10.5194/acp-14-6159-2014, 2014.

Cui, Y. Y., Liu, S., Bai, Z., Bian, J., Li, D., Fan, K., McKeen, S. A., Watts, L. A., Ciciora, S. J., and Gao, R.-S.: Religious burning as a potential major source of atmospheric fine aerosols in summertime Lhasa on the Tibetan Plateau, Atmospheric Environment, 181, 186-191, 10.1016/j.atmosenv.2018.03.025, 2018.

de Sá, S. S., Rizzo, L. V., Palm, B. B., Campuzano-Jost, P., Day, D. A., Yee, L. D., Wernis, R., Isaacman-VanWertz, G., Brito, J., Carbone, S., Liu, Y. J., Sedlacek, A., Springston, S., Goldstein, A. H., Barbosa, H. M. J., Alexander, M. L., Artaxo, P., Jimenez, J. L., and Martin, S. T.: Contributions of biomass-burning, urban, and biogenic emissions to the concentrations and light-absorbing properties of particulate matter in central Amazonia during the dry season, Atmos. Chem. Phys., 19, 7973-8001, 10.5194/acp-19-7973-2019, 2019.

DeCarlo, P. F., Kimmel, J. R., Trimborn, A., Northway, M. J., Jayne, J. T., Aiken, A. C., Gonin, M., Fuhrer, K., Horvath, T., Docherty, K. S., Worsnop, D. R., and Jimenez, J. L.: Field-Deployable, High-Resolution, Time-of-Flight Aerosol Mass Spectrometer, Analytical Chemistry, 78, 8281-8289, 10.1021/ac061249n, 2006.

Hu, W., Hu, M., Hu, W., Jimenez, J. L., Yuan, B., Chen, W., Wang, M., Wu, Y., Chen, C., Wang, Z., Peng, J., Zeng, L., and Shao, M.: Chemical composition, sources, and aging process of submicron aerosols in Beijing: Contrast between summer and winter, Journal of Geophysical Research: Atmospheres, 121, 1955-1977, 10.1002/2015jd024020, 2016.

Hu, W. W., Hu, M., Yuan, B., Jimenez, J. L., Tang, Q., Peng, J. F., Hu, W., Shao, M., Wang, M., Zeng, L. M., Wu, Y. S., Gong, Z. H., Huang, X. F., and He, L. Y.: Insights on organic aerosol aging and the influence of coal combustion at a regional receptor site of central eastern China, Atmospheric Chemistry and Physics, 13, 10095-10112, 10.5194/acp-13-10095-2013, 2013.

Jiang, H., Li, J., Sun, R., Tian, C., Tang, J., Jiang, B., Liao, Y., Chen, C. E., and Zhang, G.: Molecular Dynamics and Light Absorption Properties of Atmospheric Dissolved Organic Matter, Environ Sci Technol, 55, 10268-10279, 10.1021/acs.est.1c01770, 2021.

Jiang, H., Li, J., Tang, J., Zhao, S., Chen, Y., Tian, C., Zhang, X., Jiang, B., Liao, Y., and Zhang, G.: Factors Influencing the Molecular Compositions and Distributions of Atmospheric Nitrogen-Containing Compounds, Journal of Geophysical Research: Atmospheres, 127, 10.1029/2021jd036284, 2022.

Kaskaoutis, D. G., Grivas, G., Stavroulas, I., Bougiatioti, A., Liakakou, E., Dumka, U. C., Gerasopoulos, E., and Mihalopoulos, N.: Apportionment of black and brown carbon spectral absorption sources in the urban environment of Athens, Greece, during winter, Science of The Total Environment, 801, 10.1016/j.scitotenv.2021.149739, 2021.

Kasthuriarachchi, N. Y., Rivellini, L. H., Adam, M. G., and Lee, A. K. Y.: Light Absorbing Properties of Primary and Secondary Brown Carbon in a Tropical Urban Environment, Environ Sci Technol, 54, 10808-10819, 10.1021/acs.est.0c02414, 2020.

Lanz, V. A., Alfarra, M. R., Baltensperger, U., Buchmann, B., Hueglin, C., and Prévôt, A. S. H.: Source apportionment of submicron organic aerosols at an urban site by factor analytical modelling of aerosol mass spectra, Atmospheric Chemistry and Physics, 7, 1503-1522, 10.5194/acp-7-1503-2007, 2007.

Lei, Y., Shen, Z., Zhang, T., Lu, D., Zeng, Y., Zhang, Q., Xu, H., Bei, N., Wang, X., and Cao, J.: High time resolution observation of PM2.5 Brown carbon over Xi'an in northwestern China: Seasonal variation and source apportionment, Chemosphere, 237, 10.1016/j.chemosphere.2019.124530, 2019.

Ng, N. L., Canagaratna, M. R., Jimenez, J. L., Chhabra, P. S., Seinfeld, J. H., and Worsnop, D. R.: Changes in organic aerosol composition with aging inferred from aerosol mass spectra, Atmospheric Chemistry and Physics, 11, 6465-6474, 10.5194/acp-11-6465-2011, 2011.

Onasch, T. B., Trimborn, A., Fortner, E. C., Jayne, J. T., Kok, G. L., Williams, L. R., Davidovits, P., and Worsnop, D. R.: Soot Particle Aerosol Mass Spectrometer: Development, Validation, and Initial Application, Aerosol Science and Technology, 46, 804-817, 10.1080/02786826.2012.663948, 2012.

Qin, Y. M., Tan, H. B., Li, Y. J., Li, Z. J., Schurman, M. I., Liu, L., Wu, C., and Chan, C. K.: Chemical characteristics of brown carbon in atmospheric particles at a suburban site near Guangzhou, China, Atmospheric Chemistry and Physics, 18, 16409-16418, 10.5194/acp-18-16409-2018, 2018.

Retama, A., Ramos-Cerón, M., Rivera-Hernández, O., Allen, G., and Velasco, E.: Aerosol optical properties and brown carbon in Mexico City, Environmental Science: Atmospheres, 2, 315-334, 10.1039/d2ea00006g, 2022.

Singh, A., Rastogi, N., Kumar, V., Slowik, J. G., Satish, R., Lalchandani, V., Thamban, N. M., Rai, P., Bhattu, D., Vats, P., Ganguly, D., Tripathi, S. N., and Prévôt, A. S. H.: Sources and characteristics of light-absorbing fine particulates over Delhi through the synergy of real-time optical and chemical measurements, ATMOSPHERIC ENVIRONMENT, 252, 10.1016/j.atmosenv.2021.118338, 2021.

Sun, J., Zhang, Q., Canagaratna, M. R., Zhang, Y., Ng, N. L., Sun, Y., Jayne, J. T., Zhang, X., Zhang, X., and Worsnop, D. R.: Highly time- and size-resolved characterization of submicron aerosol particles in Beijing using an Aerodyne Aerosol Mass Spectrometer, Atmospheric Environment, 44, 131-140, 10.1016/j.atmosenv.2009.03.020, 2010.

Sun, J., Xie, C., Xu, W., Chen, C., Ma, N., Xu, W., Lei, L., Li, Z., He, Y., Qiu, Y., Wang, Q., Pan, X., Su, H., Cheng, Y., Wu, C., Fu, P., Wang, Z., and Sun, Y.: Light absorption of black carbon and brown carbon in winter in North China Plain: comparisons between urban and rural sites, Science of The Total Environment, 770, 10.1016/j.scitotenv.2020.144821, 2021.

Tian, J., Wang, Q., Ma, Y., Wang, J., Han, Y., and Cao, J.: Impacts of biomass burning and photochemical processing on the light absorption of brown carbon in the southeastern Tibetan Plateau, Atmospheric Chemistry and Physics, 23, 1879-1892, 10.5194/acp-23-1879-2023, 2023.

Ulbrich, I. M., Canagaratna, M. R., Zhang, Q., Worsnop, D. R., and Jimenez, J. L.: Interpretation of organic components from Positive Matrix Factorization of aerosol mass spectrometric data, Atmospheric Chemistry and Physics, 9, 2891-2918, 10.5194/acp-9-2891-2009, 2009.

Wang, J., Nie, W., Cheng, Y., Shen, Y., Chi, X., Wang, J., Huang, X., Xie, Y., Sun, P., Xu, Z., Qi, X., Su, H., and Ding, A.: Light absorption of brown carbon in eastern China based on 3-year multi-wavelength aerosol optical property observations and an improved absorption Ångström exponent segregation method, Atmospheric Chemistry and Physics, 18, 9061-9074, 10.5194/acp-18-9061-2018, 2018.

Wang, Q., Ye, J., Wang, Y., Zhang, T., Ran, W., Wu, Y., Tian, J., Li, L., Zhou, Y., Hang Ho, S. S., Dang, B., Zhang, Q., Zhang, R., Chen, Y., Zhu, C., and Cao, J.: Wintertime Optical Properties of Primary and Secondary Brown Carbon at a Regional Site in the North China Plain, Environmental Science

& Technology, 53, 12389-12397, 10.1021/acs.est.9b03406, 2019.
Wang, X., Chakrabarty, R. K., Schwarz, J. P., Murphy, S. M., Levin, E. J. T., Howell, S. G., Guo, H., Campuzano-Jost, P., and Jimenez, J. L.: Dark brown carbon from biomass burning contributes to significant global-scale positive forcing, One Earth, 10.1016/j.oneear.2025.101205, 2025.
Wang, Y., Hu, M., Lin, P., Guo, Q., Wu, Z., Li, M., Zeng, L., Song, Y., Zeng, L., Wu, Y., Guo, S., Huang, X., and He, L.: Molecular Characterization of Nitrogen-Containing Organic Compounds in Humic-like Substances Emitted from Straw Residue Burning, Environmental Science & Technology, 51, 5951-5961, 10.1021/acs.est.7b00248, 2017.
Washenfelder, R. A., Attwood, A. R., Brock, C. A., Guo, H., Xu, L., Weber, R. J., Ng, N. L., Allen, H. M., Ayres, B. R., Baumann, K., Cohen, R. C., Draper, D. C., Duffey, K. C., Edgerton, E., Fry, J. L., Hu, W. W., Jimenez, J. L., Palm, B. B., Romer, P., Stone, E. A., Wooldridge, P. J., and Brown, S. S.: Biomass burning dominates brown carbon absorption in the rural southeastern United States, Geophysical Research Letters, 42, 653-664, https://doi.org/10.1002/2014GL062444, 2015.
Xie, C., Xu, W., Wang, J., Wang, Q., Liu, D., Tang, G., Chen, P., Du, W., Zhao, J., Zhang, Y., Zhou, W., Han, T., Bian, Q., Li, J., Fu, P., Wang, Z., Ge, X., Allan, J., Coe, H., and Sun, Y.: Vertical characterization of aerosol optical properties and brown carbon in winter in urban Beijing, China, Atmospheric Chemistry and Physics, 19, 165-179, 10.5194/acp-19-165-2019, 2019.
Xu, J., Zhang, Q., Chen, M., Ge, X., Ren, J., and Qin, D.: Chemical composition, sources, and processes of urban aerosols during summertime in northwest China: insights from high-resolution aerosol mass spectrometry, Atmospheric Chemistry and Physics, 14, 12593-12611, 10.5194/acp-14-12593-2014, 2014.
Yue, S., Bikkina, S., Gao, M., Barrie, L. A., Kawamura, K., and Fu, P.: Sources and Radiative Absorption of Water-Soluble Brown Carbon in the High Arctic Atmosphere, Geophysical Research Letters, 46, 14881-14891, 10.1029/2019gl085318, 2019.
Yue, S., Zhu, J., Chen, S., Xie, Q., Li, W., Li, L., Ren, H., Su, S., Li, P., Ma, H., Fan, Y., Cheng, B., Wu, L., Deng, J., Hu, W., Ren, L., Wei, L., Zhao, W., Tian, Y., Pan, X., Sun, Y., Wang, Z., Wu, F., Liu, C.-Q., Su, H., Penner, J. E., Pöschl, U., Andreae, M. O., Cheng, Y., and Fu, P.: Brown carbon from biomass burning imposes strong circum-Arctic warming, One Earth, 5, 293-304, 10.1016/j.oneear.2022.02.006, 2022.
Zhang, Q., Worsnop, D. R., Canagaratna, M. R., and Jimenez, J. L.: Hydrocarbon-like and oxygenated organic aerosols in Pittsburgh: Insights into sources and processes of organic aerosols, Atmos. Chem. Phys., 5, 3289, 2005a.
Zhang, Q., Canagaratna, M. R., Jayne, J. T., Worsnop, D. R., and Jimenez, J. L.: Time and size-resolved chemical composition of submicron particles in Pittsburgh - Implications for aerosol sources and processes, J. Geophys. Res., 110, 10, 2005b.
Zhang, Q., Jimenez, J. L., Canagaratna, M. R., Ulbrich, I. M., Ng, N. L., Worsnop, D. R., and Sun, Y.: Understanding atmospheric organic aerosols via factor analysis of aerosol mass spectrometry: a review, Anal Bioanal Chem, 401, 3045-3067, 10.1007/s00216-011-5355-y, 2011.
Zhang, Q., Shen, Z., Zhang, L., Zeng, Y., Ning, Z., Zhang, T., Lei, Y., Wang, Q., Li, G., Sun, J., Westerdahl, D., Xu, H., and Cao, J.: Investigation of Primary and Secondary Particulate Brown Carbon in Two Chinese Cities of Xi'an and Hong Kong in Wintertime, Environmental Science & Technology, 54, 3803-3813, 10.1021/acs.est.9b05332, 2020a.
Zhang, Q., Shen, Z., Zhang, T., Kong, S., Lei, Y., Wang, Q., Tao, J., Zhang, R., Wei, P., Wei, C., Cui, S., Cheng, T., Ho, S. S. H., Li, Z., Xu, H., and Cao, J.: Spatial distribution and sources of winter black carbon and brown carbon in six Chinese megacities, Science of The Total Environment, 762, 143075, https://doi.org/10.1016/j.scitotenv.2020.143075, 2021a.
Zhang, X., Xu, J., and Kang, S.: Chemical characterization of submicron particulate matter (PM1) emitted by burning highland barley in the northeastern part of the Qinghai–Tibet Plateau, Atmospheric Environment, 224, 10.1016/j.atmosenv.2020.117351, 2020b.
Zhang, X., Xu, J., Kang, S., Zhang, Q., and Sun, J.: Chemical characterization and sources of submicron aerosols in the northeastern Qinghai–Tibet Plateau: insights from high-resolution mass spectrometry, Atmospheric Chemistry and Physics, 19, 7897-7911, 10.5194/acp-19-7897-2019, 2019a.
Zhang, X., Xu, J., Kang, S., Sun, J., Shi, J., Gong, C., Sun, X., Du, H., Ge, X., and Zhang, Q.: Regional Differences in the Light Absorption Properties of Fine Particulate Matter Over the Tibetan Plateau: Insights From HR-ToF-AMS and Aethalometer Measurements, Journal of Geophysical Research: Atmospheres, 126, 10.1029/2021jd035562, 2021b.
Zhang, Y., Wang, Q., Tian, J., Li, Y., Liu, H., Ran, W., Han, Y., Prévôt, A. S. H., and Cao, J.: Impact of COVID-19 lockdown on the optical properties and radiative effects of urban brown carbon aerosol, Geoscience Frontiers, 13, 101320, https://doi.org/10.1016/j.gsf.2021.101320, 2022.
Zhang, Y., Favez, O., Petit, J.-E., Canonaco, F., Truong, F., Bonnaire, N., Crenn, V., Amodeo, T., Prévôt,

A. S. H., Sciare, J., Gros, V., and Albinet, A.: Six-year source apportionment of submicron organic aerosols from near-continuous highly time-resolved measurements at SIRTA (Paris area, France), Atmospheric Chemistry and Physics, 19, 14755-14776, 10.5194/acp-19-14755-2019, 2019b.

Zhang, Y., Albinet, A., Petit, J.-E., Jacob, V., Chevrier, F., Gille, G., Pontet, S., Chrétien, E., Dominik-Sègue, M., Levigoureux, G., Močnik, G., Gros, V., Jaffrezo, J.-L., and Favez, O.: Substantial brown carbon emissions from wintertime residential wood burning over France, Science of The Total Environment, 743, 10.1016/j.scitotenv.2020.140752, 2020c.

Zhong, M., Xu, J., Wang, H., Gao, L., Zhu, H., Zhai, L., Zhang, X., and Zhao, W.: Characterizing water-soluble brown carbon in fine particles in four typical cities in northwestern China during wintertime: integrating optical properties with chemical processes, Atmos. Chem. Phys., 23, 12609-12630, 10.5194/acp-23-12609-2023, 2023.

Zhu, C.-S., Cao, J.-J., Hu, T.-F., Shen, Z.-X., Tie, X.-X., Huang, H., Wang, Q.-Y., Huang, R.-J., Zhao, Z.-Z., Močnik, G., and Hansen, A. D. A.: Spectral dependence of aerosol light absorption at an urban and a remote site over the Tibetan Plateau, Science of The Total Environment, 590-591, 14-21, https://doi.org/10.1016/j.scitotenv.2017.03.057, 2017.

Zhu, C. S., Qu, Y., Huang, H., Chen, J., Dai, W. T., Huang, R. J., and Cao, J. J.: Black Carbon and Secondary Brown Carbon, the Dominant Light Absorption and Direct Radiative Forcing Contributors of the Atmospheric Aerosols Over the Tibetan Plateau, Geophysical Research Letters, 48, 10.1029/2021gl092524, 2021.